Advanced Steel Construction – Vol. 21 No. 2 (2025) 125–135
DOI:10.18057/IJASC.2025.21.2.4

RETROFIT EFFECT AND FLEXURAL CAPACITY OF H-SECTION BEAM-THROUGH BEAM-COLUMN CONNECTIONS FOR STEEL MODULAR FRAMES

Hong-Kai Du [1], Fu-Xiong Yang [1], Yuan-Dong Wang [2,*], Peng-Fei Zhao [3] and Jin-Yu Wang [1]

[1] *Beijing Advanced Innovation Center for Future Urban Design, Beijing University of Civil Engineering and Architecture, Beijing, China*

[2] *Exyte, Salt Lake City, Utah, USA*

[3] *China Poly Real Estate Corporation Ltd., Beijing, China*

* *(Corresponding author: E-mail: matt.wang@utah.edu)*

ABSTRACT

Beam-through steel beam-column configurations are distinct from traditional column-through steel structures because they discontinue columns at each floor by bolting upper and lower columns to floor beam flanges. It facilitates modular manufacturing and floor/modular erection, which provides more opportunities for low to mid-level steel structures. Compared to its constructability superiority, beam-through configurations typically create a weaker beam-column joint than traditional beam-column connections adopted in the current building codes. In a numerical approach, this study investigates the seismic performance and flexural behavior of beam-through moment-resisting connections with H-section (wide-flange) beams and columns to improve their flexural capacity. Three beam-through moment connections are first simulated numerically and validated by quasi-static experimental tests. Then, five groups of beam-through beam-column connections are designed, calculated, and analyzed. The input parameters include stiffener thickness, doubler plate thickness, doubler plate strength, reduced beam section (RBS) depth, and multiple parameter combinations, while the main output includes yield and ultimate strength, failure mechanisms, hysteretic behavior, backbone curves, energy dissipation capacity, stiffness, ductility, and rotation, which investigates the impact of input parameters on joint flexural capacity. It discovers that increasing the stiffener plates' thickness can better enhance a beam-through joint's bending capacity. Thus, RBS reduces the load-bearing capacity of a through-beam connection and decreases the beam's capacity. However, RBS can successfully transfer the plastic hinge from the joint panel zone to the beam ends with combined with stiffener plates. Finally, an analytical method that can be used to calculate the flexural capacity of beam-through joints is also proposed.

ARTICLE HISTORY

Received: 28 May 2024
Revised: 27 December 2024
Accepted: 1 January 2025

KEYWORDS

Beam-through joint;
Steel modular moment frame;
Web doubler plates;
Reduced beam section;
Finite element analysis;
Analytical method

1. Introduction

Modular steel structures are a highly prefabricated construction system. Their advantages include standardized production, reduced erection time, short construction cycles, flexible spatial layouts, and other significant economic benefits. Prefabricated steel modular buildings have attracted more research focus and have been used in actual engineering applications in recent years [1,2]. Additionally, the prefabrication benefits make them an important structural system gradually adopted by developed countries or regions such as Europe, the United States, and Japan [3,4] due to their higher field labor cost. Beam-column joints in steel structures determine the overall structural performance, and ensure the connection reliability between modules. These joints can be categorized into column-through, diaphragm-through, and beam-through. Among them, column-through joints are the most common and widely applied, with their mechanical properties and seismic performance thoroughly investigated in the past few decades [5-7]. Meanwhile, research and engineering applications on diaphragm-through joints also increase [8-10]. However, research on beam-through joints and the optimization of the panel zone remains insufficient compared to the former two methods.

Beam-through beam-column connections are common in volumetric modular steel structures that can be utilized in low-rise to mid-rise residential and commercial buildings due to their efficiency in shop prefabrication, shop welding, and field bolted connections floor by floor [11-13]. The beam-through configuration also provides more flexibility on column locations and building plan layouts. As building industrialization progresses in eastern Asia, beam-through frame structures (BTFS) become more prevalent in China [14] and Japan [15].

Several beam-through joints have been proposed and studied previously. Chen et al. [16-18] proposed and studied tension-only concentrically braced steel beam-through frames (TCBBFs) with shake table experiments. The test results show that TCBBFs can achieve uniform story drift response with self-centering ability upon loading, which can be easily replaced after major earthquakes. Wang et al. [12] further analyzed the TCBBFs as mentioned above experimentally and numerically and found that the TCBBFs structure was stable at an inter-story drift of 1/10. Then, Yao et al. [13] improved the TCBBFs with eccentrical layout and showed that eccentrically braced beam-through steel frames with replaceable shear links also improved the frames' energy dissipation capacity, stiffness, ultimate capacity, and ductility.

Similarly, Hu et al. [19,20] examined the seismic performance of a beam-through tension-only concentrically braced frame with energy-absorbing rocking core (ERC), which indicated that ERC could control the maximum residual drift within 0.5%. Furthermore, Zhang et al. [21] introduced a combined system of friction spring-based self-centering (SC) devices and self-centering rocking cores (SRC) to improve the resilience of beam-through frames. The proposed system reached target seismic performance under near-field and far-field ground motions by effectively controlling seismic displacement and deformation.

Li et al. [22,23] introduced a beam-through steel frame with T-type curved knee braces (TCKBs) to provide stable strength and full energy dissipating capacity. In addition, Li et al. [24] proposed a beam-through configuration for the connections between steel frames and energy-dissipative rocking columns (EDRCs) to minimize the necessary workload when using EDRCs. The numerical analyses proved that beam-through EDRCs provide satisfying lateral resistance and energy dissipation capacities. Similarly, Jeddi et al. [25] proposed a novel moment-resisting connection named a through rib stiffener beam connection, which is directly passed through a pre-slotted circular column with concrete fill. Thus, Jamali et al. [26] provided a revised H-section beam and boxed column joint with two through stiffener plates, indicating the effects of the through stiffener plates on improving seismic performance.

Since beam-through joints at H-section beams and columns tend to have insufficient capacity in the joint core area, it is common to reinforce the joint area to improve seismic performance. For instance, Chen et al. [27] compared the seismic behaviors of beam-through H-section beam-column joints and traditional column-through joints. It showed that small bolt group slippage can provide better hysteretic behavior, and the beam flange and web thickness significantly affect the joint's ultimate capacity. Tagawa and Gurel [28] utilized stiffener plates to reduce the tensile deformation at column flanges, and added web doubler plates to prevent shear failure of beam-through core joint. Likewise, Zhong et al. [29] found that the changes in stiffener thickness in the panel zone have significant effects on the joint's ultimate rotation capacity and ductility. Čermelj et al. [30] analyzed the low-cycle fatigue behaviors of rib-stiffened (RS) and cover plate (CP) connections, which proved the superiority of CP over RS connections. Ma et al. [31] demonstrated the efficiency of double stiffener plates at H-shaped beam-through beam and column connections in improving joint strength and ductility.

Besides adding double plates in the beam-column joint, it is also common and seismically efficient to introduce reduced beam section (RBS), significantly improving joint deformation and ductility [32]. Chen et al. [33] proposed beam-to-column moment connections with reduced beam sections. The experimental tests proved that with RBS, the ultimate joint capacity remained the same, joint stiffness slightly degraded, and plastic rotation capacity increased dramatically. Furthermore, Sophianopoulos and Deri [34] investigated the influence of RBS configuration, dimensions, locations, and lateral bracing on beam-column joint seismic performance. Carter and Iwankiw [35] demonstrated that trapezoidal RBS at concave corners might trigger stress concentration, while curve RBS can generate satisfactory plastic performance and provide more ductility. Thus, Jones et al. [36] verified the seismic performance of the RBS beam-column joint by performing experimental tests. Seven groups of specimens reached a rotational angle of 0.04 rad before stiffness degradation occurred.

In addition, Lee et al. [37] found that plastic hinges are prone to be developed in the RBS with regular beam-column joint web stiffnesses when the joint rotation reached 0.01 rad, while Wang et al. [38] found that the ultimate joint rotation with RBS welded beam-column joint could reach a rotational angle of 0.077 rad. In follow-up studies, Chen et al. [39] provided optimal design parameters for RBS connections, and Roudsari et al. [40] showed the contribution of web stiffeners to the seismic performance of beam-column joints with RBS. However, in numerical approaches, no previous study has considered combining beam-through beam-column moment connections with RBS, stiffeners, and doubler plates.

This study proposes cruciform beam-column moment connections with steel H-sections (wide-flanges), as shown in Fig. 1. On contratry to traditional beam-column connections, moment frame beams remain continuous while columns are connected to the top and bottom flanges of through-beams. It starts with validating the numerical model of beam-through beam-column moment connections with previous experimental test data under a quasi-static loading protocol. The second phase is to numerically optimize the design input parameters for beam-through beam-column connections, including stiffener plate thickness, doubler plate thickness, doubler plate strength, RBS, and multiple parameter combinations. One key objective is to understand and optimize the design methods on the flexural capacity of beam-through joints. Finally, a novel analytical method and equations are proposed to calculate beam-through beam-column connections' flexural behavior and capacity.

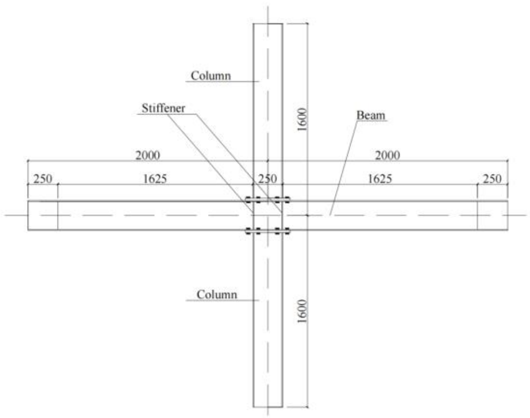

(a) Configuration

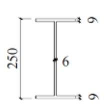

(b) Beam and column section

Fig. 1 Specimen dimensional sections (unit: mm)

2. FEM modeling and experimental validation

The finite element model (FEM) analyses are in ABAQUS to numerically evaluate the seismic performance of beam-through beam-column connections. The FEM tests are first validated by previous cyclic experimental tests under quasi-static loading protocols [32].

2.1. Specimen and test design

Three steel cross beam-through joint assemblages are designed with identical sizes and dimensions. The beam length is 4000 mm (13.12 ft), and the column height is 3200 mm (10.5 ft). The same W-section (wide flange) following the China specifications GB/T 11263-2017 [41] HN250×125×6×9 (Fig. 1) that is equivalent to AISC W10x22 [42] is utilized in the beams and columns for all specimens. Each joint has bolted stiffened end plate at the column flange. Three specimens are named SFT-6, DPT-6, and RBS-30, as shown in Table 1. Fig. 2 presents the critical design parameters for SFT-6, whose panel zone area has two welded 6 mm (1/4 in) thick stiffeners on each side (four in total). DPT-6 incorporates a panel zone doubler plate (6 mm [1/4 in]) welded at the nine 16 mm (0.63 in) welding holes and perimeters, as in Fig. 3. Thus, RBS configuration is included in the same design as SFT-6, namely RBS-30. The RBS is located 80 mm (3.15 in.) to the column flange, and the reduced section cut curve length, depth, and radius is 180 mm (7.067 in), 30 mm (1.181 in), and 150 mm (5.906 in), respectively (Fig. 4).

All steel material is Chinese Q235, which has a yield strength of 235 MPa (34 ksi) [44]. Table 2 summarizes the average properties for the steel samples that were cut from the beams, columns, continuity plate stiffeners, and end plates, which are higher than the code-required yield strength. All experimental tests for this study were performed at the structural lab, Beijing University of Civil Engineering and Architecture. All tested columns were fixed to the structural test frame at both ends by through-bolted connections. The axial force was applied at the column end to maintain a compressive axial ratio of 0.3 by three electro-hydraulic actuators, and quasi-static loading was applied simultaneously at the beam ends in opposite directions. The test setup is shown in Fig. 5, and the experimental loading protocol is shown in Fig. 6.

2.2. Finite element model

The finite element (FE) model overview is shown in Fig. 7, which has the same dimensions as those experimental specimens specified in section 2.1. Eight-node linear hexahedral elements with reduced integration and hourglass control (C3D8R) in ABAQUS are used to mesh all the members. Finer meshes are applied to the beam-through web, beam flanges, and stiffener plates. The mesh size along the beam and column length direction is 60 mm ×49 mm (2.36 in ×1.93 in), the mesh size in the panel zone area is 7 mm ×16 mm (0.28 in ×0.63 in), and the thickness mesh is 2 mm (0.079 in). Since no significant damage is observed at the connection bolts, bolts and nuts are modeled by ignoring the threads' impact. The FE assembly of all components is shown in Fig. 8. Surface-to-surface contact method of ABAQUS is adopted at the column end plates, bolts, and beams. Beam stiffener plates, beam, column, column end plates, and doubler plates are welded together and simulated by the tie method in ABAQUS.

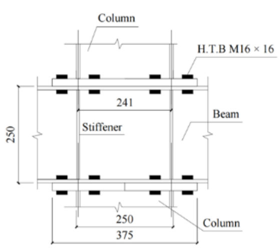

(a) Front elevation view

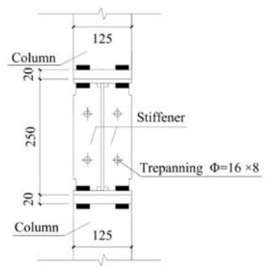

(b) Right section view

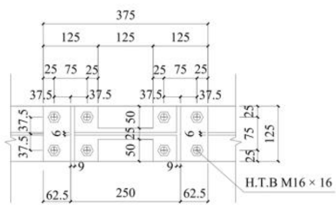

(c) Plan view

Fig. 2 SFT-6 panel zone details (unit: mm)

Table 1
Experimental specimen characteristics

No.	Name	Characteristics
1	SFT-6	Standard H-section beam-through joint with 6 mm (0.236 in) stiffener plates
2	DPT-6	SFT-6 with a 6 mm (0.236 in) web doubler plates in the panel zone
3	RBS-30	SFT-6 with 30 mm (1.18 in) deep RBS at beam ends

Note: These are the three experimental specimens, which are also used in numerical modeling. See Table 4 for the naming definition.

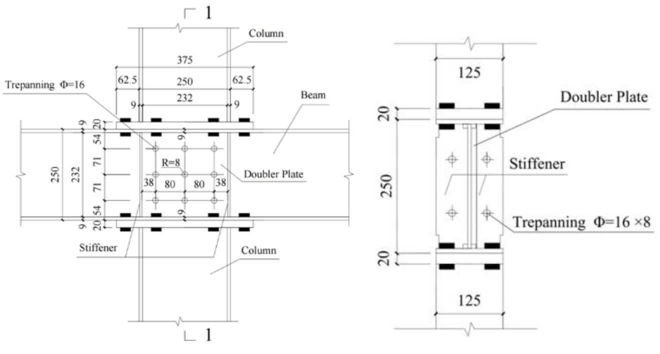

(a) Configuration (b) Beam and column section

Fig. 3 Specimen dimensional sections (unit: mm)

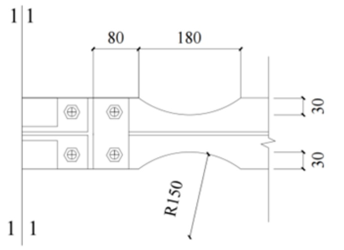

Fig. 4 RBS-30 beam flange dimensional detail (unit: mm)

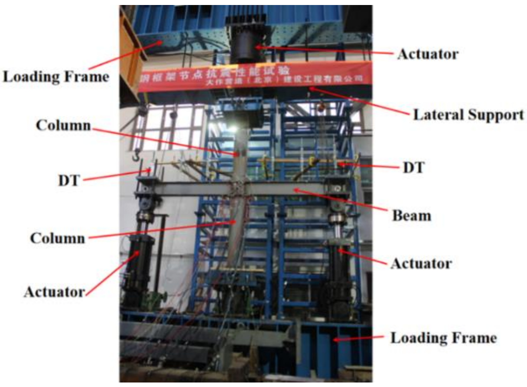

(a) Test picture

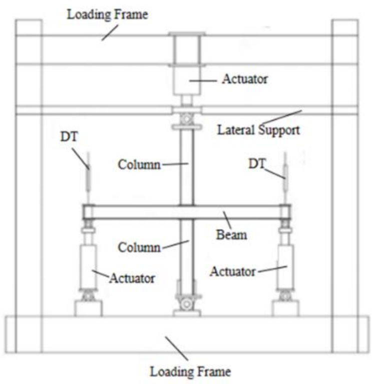

(b) Test sketch

Fig. 5 Experimental setup

Other FEM setup includes a bilinear kinematic hardening material model to model steel elastoplastic deformations from component experimental tests. The bolt pretension force is modeled by the bolt loading modulus, i.e., 107 kN (24 kips) for M16 bolts utilized in this study. Coupling points are set at both the column and beam ends that define the member section properties. The column's bottom-end boundary condition is defined as pin while the column's top end is described as a roller that allows all the rotation and vertical movement. Same boundary conditions are established at the beam ends as the column's miming the experimental testing setup. Finally, the ABAQUS/Standard solver is applied in analyzing the numerical models.

The bolt pre-loading process is divided into three stages under different load magnitudes to improve the FE analysis convergence. Firstly, only 10 N (2.25 LBS) is applied to the bolts to trigger acceptable contact between the bolts and other elements. Then, full loading is imposed, and the bolt loading is modified from force-based to a fixed length, which simulates the pretension effects. Column axial forces and beam cyclic loads are also applied simultaneously during the numerical analysis till the end of the numerical loading process.

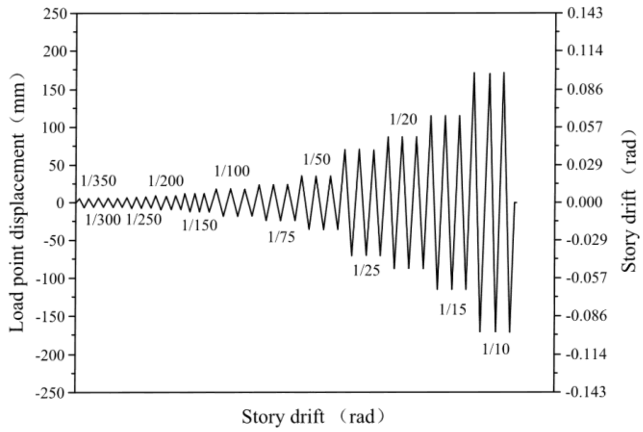

Fig. 6 Beam ends loading protocol

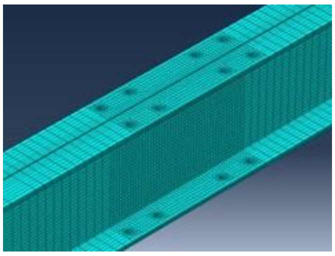

(a) Beam

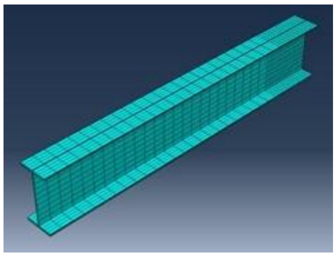

(b) Column

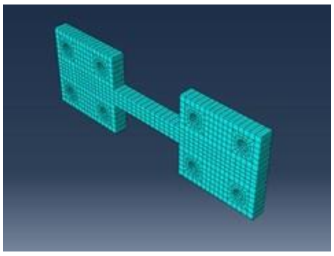

(c) End plate

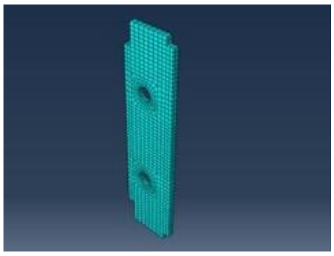

(d) Stiffener

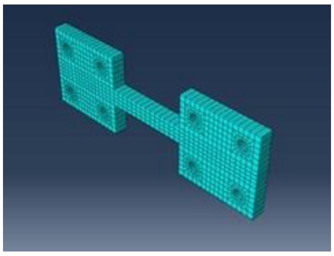

(e) Bolt

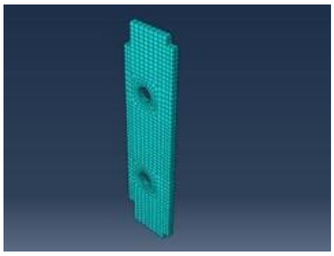

(f) Doubler plate

Fig. 7 FEM component meshing in beam, column, stiffeners, and doubler plates

2.3. Model validation

The comparison of numerical and experimental failure modes is shown in Fig. 9. Main damage features observed in the experimental tests can be well simulated by the FE model for all three specimens (STF-6, DPT-6, and RBS-30). Take specimen STF-6 as an example. The beam-column panel zone is yielded by exceeding a strength of 368 MPa (53.4 ksi) when reaching a joint rotation of 0.013 rad (1/75) in the FE analysis, which matches the same progress in the experimental test. As in the experimental test, the 45° buckling deformation in the panel zone further develops, stiffener plates start to bend, and plasticity occurs at the column flange and end plates when rotation angle increases to 0.1 rad (1/10) (Figs. 9a and 9b).

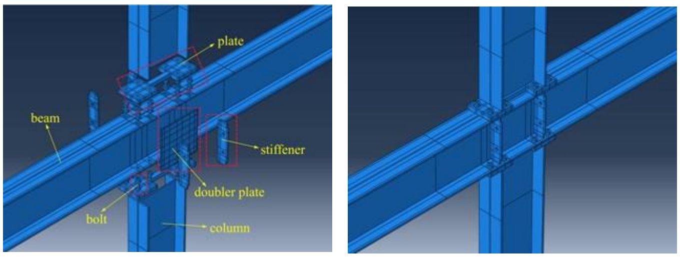

(a) Element decomposition (b) Assembly

Fig. 8 FEM component meshing

In specimen DPT-6, diagonal bulges appear in the panel zone with the rotation angle raised to 0.067 rad (1/15), which also meets the experimental behavior. Compelling yielding deformation can be seen at the beam flanges and column end plates under the same loading magnitude. Once the stiffener plates yields, column flanges also start yielding near the end plate, as in Figs. 9c and 9d. Similarly, the RBS-30 numerical simulation also predicts the experimental specimen test well (Figs 9e and 9f).

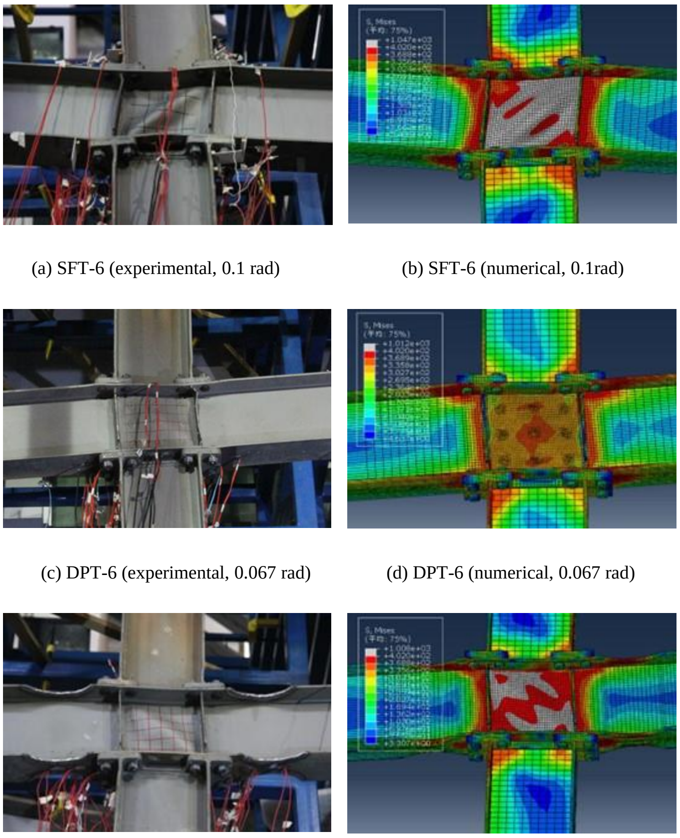

(a) SFT-6 (experimental, 0.1 rad) (b) SFT-6 (numerical, 0.1rad)

(c) DPT-6 (experimental, 0.067 rad) (d) DPT-6 (numerical, 0.067 rad)

(e) RBS-30 (experimental, 0.067 rad) (f) RBS-30 (numerical, 0.067 rad)

Fig. 9 Comparison of numerical and experimental results

The comparison of load-displacement curves is presented in Fig. 10. Both experimental and numerical results show the exact buckling directions and magnitudes in the panel zone area once the beam-through web yields. Similarly, the experimental and numerical moment-rotation angle curves demonstrate close mechanical behavior and performance.

Backbone curve analyses and curve-fitting are applied to both experimental and numerical results to get the elastic stiffness, yield point, yield strength, yield displacement, and ultimate strength, as summarized in Table 3. As observed, the difference between the two is less than 15%, with an average error or difference of 10%. These errors may originate from the boundary conditions of the test model setup. During the experimental tests, it is challenging to constrain the out-of-plane deformation. Therefore, this out-of-plane deformation reduces the test load while amplifying the test displacement, resulting in a test load lower than the simulated load and a test displacement greater than the displacement from numerical analyses. Even though there may be some imperfections or errors in the numerical simulation, it still maintains a high degree of accuracy, which indicates the accuracy and satisfaction of the numerical model for subsequent analyses. As shown in Table 3, the ultimate inter-story drifts of all three specimens exceed 0.04 rad, which is higher than the drift ratios required by the current building codes (e.g., AISC 341 [43]). As noted, all three beam-column joints fail in the joint panel zone, which is not preferable per the current codes.

Table 2
Material property parameters of experimental specimens

Part	Density ρ (kg /m^3)	Elastic Modulus E (MPa)	Yield Strength f_y (N /mm^2)	Ultim. Strength f_u (N/mm^2)	Elongation ε_u
M16 bolt	7850	207510	906	1100	0.089
Beam	7850	207460	369	618	0.249
Column	7850	203880	338	606	0.263
Doubler plate	7850	214220	271	471	0.238
Stiffener	7850	204473	299	528	0.235

Table 3
Numerical and experimental results comparison

Name	Yield displacement (mm)			Yield strength (kN)			Elastic stiffness (kN/m)		
	Exper.	Numer.	Diff.	Exper.	Numeri.	Diff.	Exper.	Numer.	Diff.
SFT-6	23.77	20.8	-12.5%	27.1	27.27	0.5%	1616.4	1698.5	5.1%
DPT-6	29.39	27.0	-8.2%	37.4	42.65	14.5%	1715.5	1898.1	10.6%
RBS-30	23.86	21.7	-9.2%	26.9	27.36	2.5%	1629.4	1626.9	0.2%

Note: $diff. = \frac{Numer. - Exper.}{Exper.}$

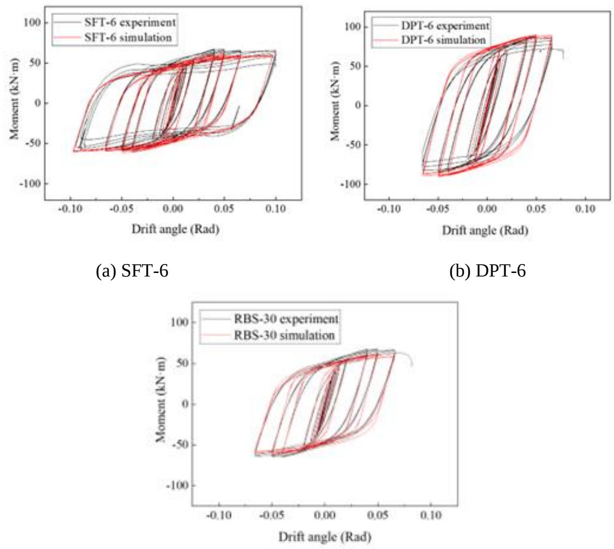

(a) SFT-6 (b) DPT-6

(c) RBS-30

Fig. 10 Comparison of experimental and numerical hysteresis curves

3. Numerical parametric study

In this section, five design or strengthening methods are numerically considered to address the inadequacy of flexural capacity at the panel zone of beam-through beam-column connections. It might even cause global collapse [44,45], starting with local buckling in unbraced flexural members. Therefore, stiffener plates (SFT), doubler plate thickness (DPT), doubler plate strength (DPS), and reduced beam section (RBS) are the main input parameters to improve the flexural capacity in the panel zone. Thus, combinations of the three methods are also included in this study as combinatorial (COM) components further to investigate the seismic performance of beam-through beam-column connections. Herein, COM-a includes doubler plates, COM-b incorporates RBS configurations, and COM-c encompasses both doubler plates and RBS. In total, five groups of specimens are designed accordingly (Table 4) [46]. All numerical input parameters are directly adopted from previous component experimental tests. Also, the loading methods and loading protocol follow the same experimental setup.

3.1. SFT analysis

Five beam-through joints (SFT-2, SFT-4, SFT-6, SFT-8, and SFT-10) are proposed with different stiffener plate thicknesses, which are 2 mm (0.079 in), 4 mm (0.157 in), 6 mm (0.236 in), 8 mm (0.315 in), and 10 mm (0.394 in), as shown in Table 4. Correspondingly, SFT-2 denotes the joint specimen with 2 mm stiffener plates. As observed, the joint panel zone yields when the rotation angle reaches 0.04 rad, and plate buckling occurs in all five specimens under the 0.067 rad rotation (Fig. 11). The stiffener plates yield in specimens SFT-2 and SFT-4, while no stiffener plates yielding is observed in the other three specimens. It indicates that the strengthening effects increase with the stiffener plate thickness.

Table 5 presents the ultimate moment capacity and total dissipated energy for all five specimens by interpreting the output hysteretic and backbone curves. Fig. 12 presents the backbone curves for all five SFT specimens, whose elastic stiffness and yield points are close. Once SFT specimens yield, all five post-yield curves almost match except SFT-2, whose post-yield curve is a little lower. Compared to SFT-6, whose stiffener and column flange thicknesses are the same, all the other specimens have similar moment and dissipated energy capacity with a difference of less than 2% and 6%, respectively. This phenomenon proves that even though thicker stiffener plate prevents undesirable buckling behavior, thicker stiffener plates have negligible effects on the joint flexural capacity. The panel joint shear capacity provides the flexural behavior of the beam-through joint, while the stiffener plates and the top of the bottom beam flanges form a rectangle that adds limited flexural capacity. However, the stiffener plates between beam-through flanges transfer the vertical forces through beam-column joints, significantly improving the connection integrity. In this study, 6 mm (0.236 in) is the thickest stiffener plate that yields, while the column web thickness is 6 mm (0.236 in). Therefore, the beam-through panel joint stiffener plate thickness should not be smaller than the larger column web thickness.

Table 4
Specimen design detail

Group	No.	Beam/Column Section (mm)	Stiffener thickness (mm)	Doubler plate thickness (mm)	Doubler plate strength (MPa)	RBS depth (mm)	Note
	SFT-2		2				-
	SFT-4		4				-
Stiffener thickness	SFT-6	250×125×9×6	6	0	0	0	Tested
	SFT-8		8				-
	SFT-10		10				-
	DPT-2			2			-
	DPT-4			4			-
Doubler plate thickness	DPT-6	250×125×9×6	6	6	300	0	Tested
	DPT-8			8			-
	DPT-10			10			-
	DPS-300				300		Same as DPT-6
Doubler plate strength	DPS-360	250×125×9×6	6	6	360	0	-
	DPS-420				420		-
	RBS-30					30	Tested
Reduced beam section	RBS-40	250×125×9×6	6	6	300	40	-
	RBS-50					50	-
	RBS-55					55	-
	COM-a			8		0	Same as DPT-8
Combinatorial	COM-b	250×125×9×6	6	0	300	40	-
	COM-c			8		40	-

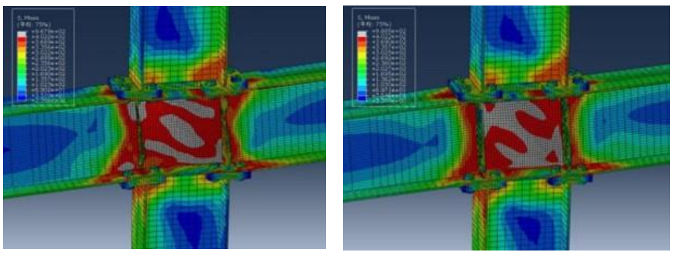

(a) SFT-2 (b) SFT-6

Fig. 11 Group SFT Stress distribution at 0.067 rad

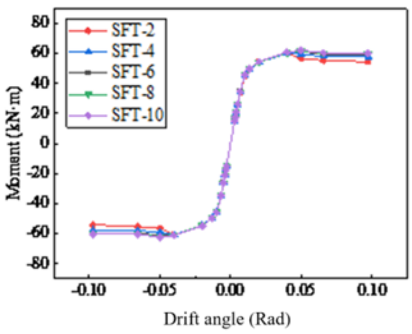

Fig. 12 Group SFT backbone curves

3.2. DPT analysis

This section examines the influence of doubler plates on the seismic performance of beam-through joints. Besides the 6 mm (0.236 in) stiffener plates (i.e., DPT-6), doubler plates with five thicknesses (i.e., 2 mm [0.079 in], 4 mm [0.157 in], 6 mm [0.236 in], 8 mm [0.315 in], and 10 mm [0.394 in]) are also included in the numerical model. See Table 4 for more details. The number in the specimen's name represents the doubler plate thickness. For instance, DPT-2 has 2 mm (0.079 in) thick doubler plates.

Table 5
Numerical results - group SFT

Name	Values					Increment ratio (to SFT-6)			
	SFT-2	SFT-4	SFT-6	SFT-8	SFT-10	SFT-2	SFT-4	SFT-8	SFT-10
Ultimate Moment (kN · m)	60.47	60.5	61.56	62	62.29	-1.77%	-1.72%	0.71%	1.19%
Total dissipated energy (KJ)	111.3	115.45	118.64	120.28	120.9	-6.19%	-2.69%	1.38%	1.90%

As shown in Fig. 13, doubler plate thickness substantially affects the panel zone deterioration and failure under quasi-static and cyclic loading protocols. Under a joint rotation angle of 0.013 rad, the panel zone web stress dramatically decreases with the increase of doubler plate thickness. The stress is highest in DPT-2 and lowest in DPT-10. When the joint rotational angle increases to 0.067 rad, buckling occurs in DPT-2 and DPT-6, while no apparent buckling is observed in DPT-10. The backbone curves of all five DPT specimens are shown in Fig. 14. Once the beam-column joints yield, the joint's secondary stiffness increases as the doubler plate thickness.

Table 6 compiles the yield displacement, yield moment, ultimate moment, and total dissipated energy for all five specimens. Again, the results prove that the doubler plate increases the panel zone capacities. The yield rotational angle of DPT-8 and DPT-10 increases 9.09% and 14.29% from DPT-6, the yield moment of DPT-8 and DPT-10 increases 7.57% and 12.93% from DPT-6, and the ultimate moment of DPT-8 and DPT-10 increases 10.77% and 17.38 % from DPT-6. Considering the material property, the overall panel zone thickness with doubler plate for DPT-8 and DPT-10 increases by 16.7% and 33.3% from DPT-6. Thus, doubler plates increase the shear strength of the panel zone and the out-of-plane moment of inertia for the beam-through web.

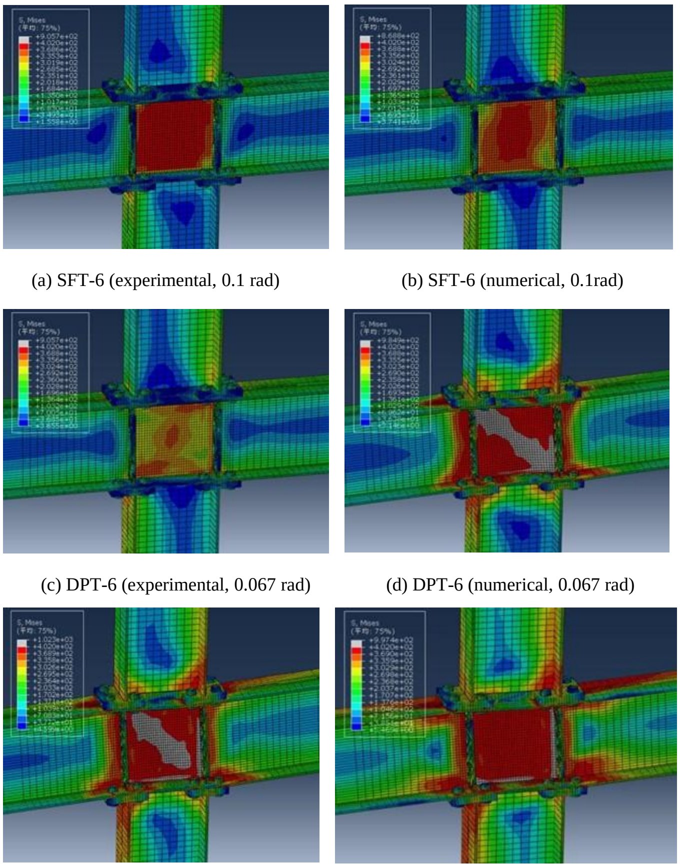

(a) SFT-6 (experimental, 0.1 rad) (b) SFT-6 (numerical, 0.1rad)

(c) DPT-6 (experimental, 0.067 rad) (d) DPT-6 (numerical, 0.067 rad)

(e) RBS-30 (experimental, 0.067 rad) (f) RBS-30 (numerical, 0.067 rad)

Fig. 13 Group DPT stress distribution

A linear correlation can be found between the doubler plate thickness and corresponding beam-column joint capacities, such as yield moment and ultimate moment. In this study, r_{My} denotes the nominal yield moment of a specimen (e.g., DPT-8) over DPT-6, r_{Mu} represents the nominal ultimate moment of a specimen (e.g., DPT-8) over DPT-6, and r_{DPT} is the nominal doubler plate thickness of a specimen (e.g., DPT-8) over DPT-6. The relationship among r_{My}, r_{Mu}, and r_{DPT} can be summarized as Eqs. 1 and 2 by analyzing the numerical results.

$$r_{My} = 0.27r_{DPT} + 0.70 \tag{1}$$

$$r_{Mu} = 0.30r_{DPT} + 0.69 \tag{2}$$

The total dissipated energy for all five specimens shown in Table 6 shows that the energy dissipated by DPT-2 and DPT-4 is reduced by 18.57% and 9.90%, compared to DPT-6, while the energy dissipated by DPT-8 and DPT-10 increases by 3.80% and 3.2%. The limited improvement of energy dissipation for DPT-8 and DPT-10 is due to the limited yielding development in the panel zone area for 8 mm and 10 mm thick doubler plates (i.e., DPT-8 and DPT-10). Therefore, increasing doubler plate thickness can productively increase the beam-through joint capacity but has negligible effects on the energy dissipation capacity due to the limited yielding developed.

Table 6
Numerical results - group DPT

Name	Values					Increment ratio (to DPT-6)			
	DPT-2	DPT-4	DPT-6	DPT-8	DPT-10	DPT-2	DPT-4	DPT-8	DPT-10
Yield rotation angle (rad)	0.0128	0.014	0.0154	0.0168	0.0176	-16.88%	-9.09%	9.09%	14.29%
Yield moment (kN · m)	57.5	66.84	74.64	80.29	84.29	-22.96%	-10.45%	7.57%	12.93%
Ultimate moment (kN · m)	70.5	80.15	90.1	99.8	105.76	-21.75%	-11.04%	10.77%	17.38%
Total dissipated energy (KJ)	80.86	89.47	99.3	103.07	102.48	-18.57%	-9.90%	3.80%	3.20%

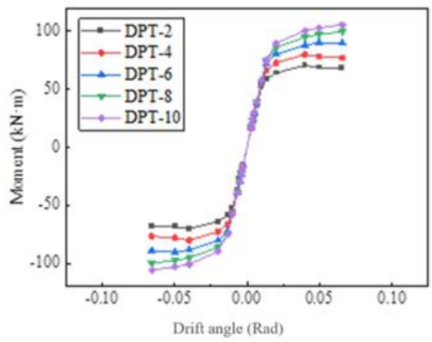

Fig. 14 Group DPT backbone curves

3.3. DPS analysis

Three doubler plate yield strengths (DPS-300, DPS-360, and DPT-420) are studied in this section, which are 300 MPa (43.5 ksi), 360 MPa (52.2 ksi), and 420 MPa (60.9 ksi), as shown in Table 4. DPS-300 denotes the specimen with doubler plates with 300 MPa (43.5 ksi) yield strength. Fig. 15 shows the stress distribution of doubler plates under a joint rotation angle of 0.067 rad. As noted, different plate strength does not impact the plate bulking or stress distribution in the panel zone area stiffened by doubler plates. Fig. 16 shows the backbone curves of all three specimens, where the maximum inter-story drift exceeds 0.05.

Table 7 presents the yield displacement, yield moment, and ultimate moment shown in the three specimens. The yield moment of DPS-360 and DPS-420 is improved by 4.90% and 9.45% from DPS-300, respectively. The yield moment of DPS-360 and DPS-420 increases by 5.18% and 10.0%, with the same doubler plate strength increase of 20% and 50%. Therefore, improving doubler plate strength can slightly improve the seismic performance of beam-through beam-column connections. Finally, the yield moment and ultimate moment ratio for these three specimens with different doubler plate strengths can be summarized below, where r_{DPS} is the strength ratio of a doubler plate over DPS-300.

The same minor improvement of seismic performance by raising the doubler plate strength (by 20% and 50%) can also be observed for the total dissipated energy (only increased by 1.44% and 1.98%) in Table 7. This improvement is due to the limited yielding development in the three specimens designed in this section. In summary, increasing stiffener thickness can restrict the buckling behavior of the panel zone and fully utilize steel's strength and ductility. However, merely improving steel strength is less efficient in leveraging its ultimate strength once buckling occurs in the panel zone. However, increasing doubler plate thickness is more efficient than increasing doubler plate strength since r_{My} and r_{Mu} are 0.27 and 0.30 for doubler plate thickness and 0.24 and 0.25 for doubler plate strength.

$$r_{My} = 0.24r_{DPS} + 0.76 \tag{3}$$

$$r_{Mu} = 0.25r_{DPS} + 0.75 \tag{4}$$

Table 7
Numerical results - group DPS

Name	Values			Increment ratio (to SFT-6)	
	DPS-300	DPS-360	DPS-420	DPS-360	DPS-420
Yield rotation angle (rad)	0.0154	0.0162	0.017	5.19%	10.39%
Yield moment (kN · m)	74.64	78.3	81.69	4.90%	9.45%
Ultimate moment (kN · m)	90.09	94.76	99.1	5.18%	10.00%
Total dissipated energy (KJ)	99.3	100.73	101.26	1.44%	1.97%

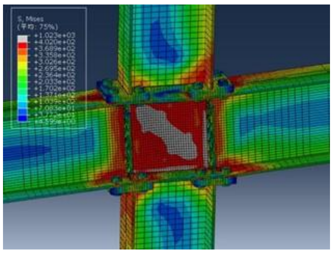

(a) DPS-300 (0.067 rad)

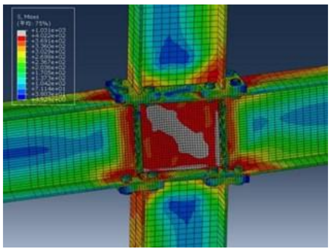

(b) DPS-360 (0.067 rad)

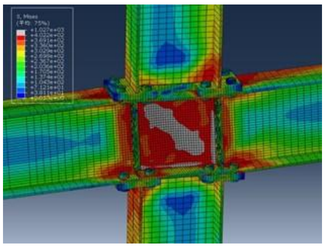

(c) DPS-420 (0.067 rad)

Fig. 15 Group DPS stress distribution

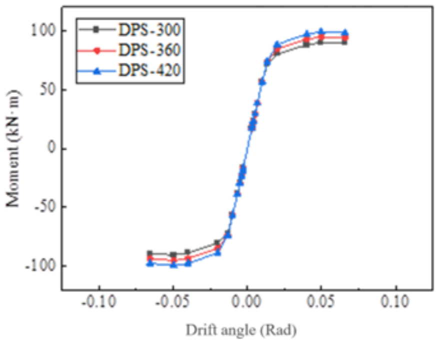

Fig. 16 Group DPT backbone curves

3.4 RBS analysis

The RBS joints are designed following the AISC prequalified connection [47]. The cut curve length and radius are 180 mm (7.067 in) and 150 mm (5.906 in), and the cut curve depths are 30 mm, 40 mm, 50 mm, and 55 mm, which are named RBS-30, RBS-40, RBS-50, and RBS-55. Correspondingly, the beam-through flange is reduced by 48%, 64%, 80%, and 88%, respectively.

The mises stress contour for all four specimens are shown in Fig. 17. All specimens' panel zone reaches yield strain under a joint rotation angle of 0.04 rad. However, the stress distribution near the RBS web is different. With the cut curve length and radius increase, the web stress also greatly increases. When the rotational angle is at 0.067 rad, the RBS web starts buckling, and the panel zone stress slightly decreases. However, no apparent buckling is observed at the other RBS joints' web or flanges.

Fig. 18 shows the backbone curves for all four RBS specimens, which are close before reaching a rotational angle of 0.04 rad. RBS-55 starts to yield and fail after reaching a rotational angle of 0.04 rad, and the post-yielding capacity is only 68.2% of the peak capacity. As noted, plastic hinges may occur at the reduced sections, and panel zone of beam-through joints. When the cut depth is too small, it is tough to develop plastic hinges at the reduced sections, and the joint seismic performance is like that of a panel zone without RBS. In this study, plastic hinges occur only when the beam cut depth is reduced by 88%. In summary, an RBS design can relocate the occurrence of plastic hinges and undermine the beam's flexural capacity, which is only recommended if reinforcing the panel zone web with doubler plates.

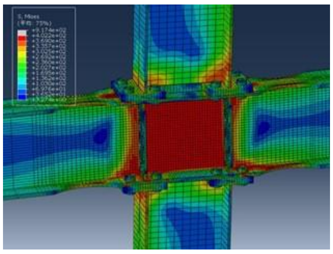

(a) RBS-30 (0.04 rad)

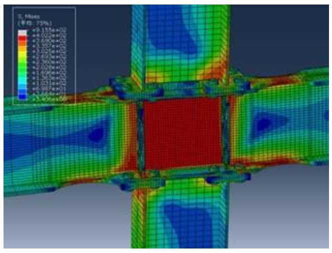

(b) RBS-40 (0.04 rad)

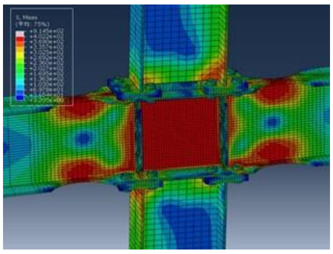

(c) RBS-50 (0.04 rad)

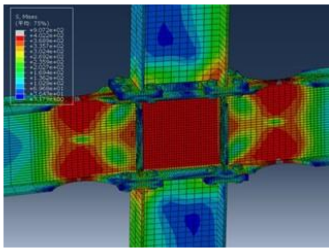

(d) RBS-55 (0.04 rad)

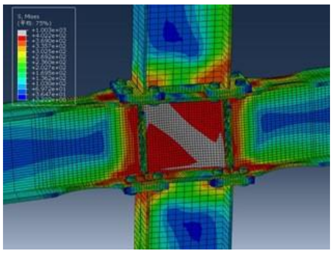

(e) RBS-30 (0.067 rad)

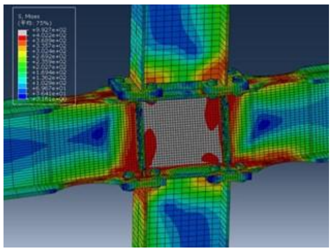

(f) RBS-40 (0.067 rad)

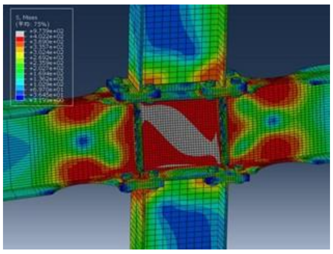

(g) RBS-50 (0.067 rad)

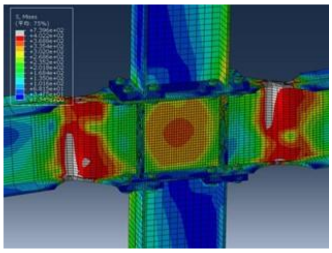

(h) RBS-55 (0.067 rad)

Fig. 17 Group RBS stress distribution

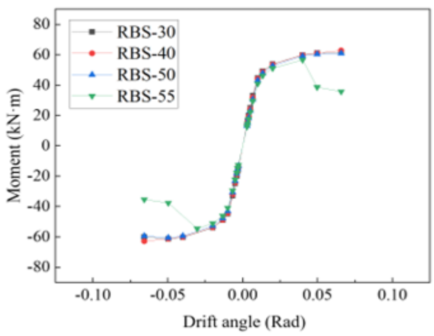

Fig. 18 Group RBS backbone curves

3.5. COM analysis

Three COM (combinational) specimens are designed to find the optimal flexural performance for beam-through beam-column connections. The design parameters are shown in Table 4. All three specimens have 6 mm (0.236 in) stiffener plates to better transfer the gravity load through the beam-through connections from level to level. COM-a includes an 8 mm (0.315 in) doubler plate, COM-b incorporates a 40 mm (1.57 in) deep RBS section cut, and COM-c combines COM-a and COM-b.

The stress distribution of all specimens is shown in Fig. 19. The beam-through panel zone for COM-a and COM-c does not reach flexural strength with a rotational angle is 0.013 rad incorporating the strengthening effects of doubler plates, while the beam-through web for COM-b yields. The peak stress in the COM-c's panel zone is reduced by including RBS compared to that of COM-a, which demonstrates that both RBS and doubler plates can effectively reduce the panel zone stress. As observed in Figs. 19d, 19e, and 19f, only specimen COM-C (doubler plate + RBS) effectively shifts the plastic hinge from the panel zone to the beam ends, while COM-a (doubler plate only) and COM-b (RBS only) still maintain significant plastic deformation in the joint panel zone.

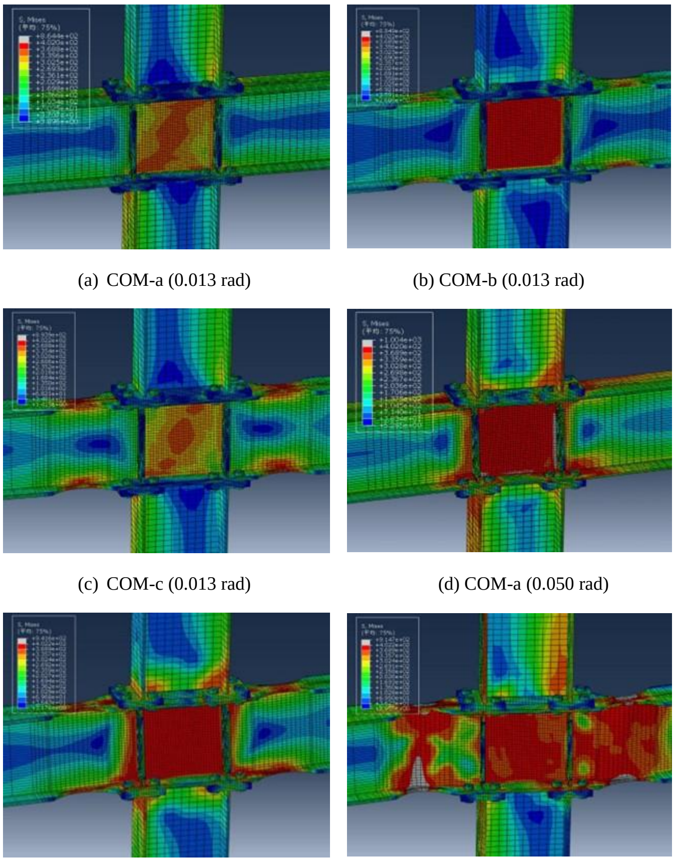

(a) COM-a (0.013 rad) (b) COM-b (0.013 rad)

(c) COM-c (0.013 rad) (d) COM-a (0.050 rad)

(e) COM-b (0.050 rad) (f) COM-c (0.050 rad)

Fig. 19 Group RBS stress distribution

Fig. 20 summarizes the backbone curves for all three COM specimens. Doubler plates can significantly increase the flexural capacity of beam-through beam-column connections. The design capacity of COM-c is reduced once the inter-story drift reaches 0.04 rad, while COM-a does not because plastic hinges occurred at RBS. The occurrence of plastic hinges delays the panel zone buckling and avoids global structural collapse. The Chinese code [38] requires a maximum inter-story drift angle of 0.02 rad, which both COM-a and COM-c meet. It proves the efficiency of RBS in beam-through beam-column moment connections, even though it fails earlier than those specimens without RBS.

The seismic parameter and failure modes are listed in Table 8. The panel zone design of specimens COM-c and COM-a is identical, while COM-c adopts RBS configurations. The ductility and flexural capacity of COM-c decreases by 10.1% and 19.1% from COM-a, respectively. As discussed earlier, the RBS configuration in COM-C has successfully shifted the plastic hinge and weak point to the beam ends. It indicates that the ductility and flexural capacity reduction are from the RBS design. However, even though COM-b also has an RBS configuration, RBS is ineffective due to its design parameter, and the primary failure still occurs in the joint panel zone. In actual engineering design, this study recommends engineers calculate and utilize the smaller capacity of joint panel zone and RBS, which aims to fulfill the functionality of RBS configuration.

Table 8
Numerical results - group COM

Name	Dou-bler plates	RBS	Failure loca-tion	F_y (kN)	Δ (mm)	F_u (kN)	Δ_{max} (mm)	μ
COM-a	Yes	No	Panel Zone	45.88	29.38	56.97	115.0	3.91
COM-b	No	Yes	Panel Zone	27.62	22.74	35.92	115.0	5.06
COM-c	Yes	Yes	RBS	41.26	27.72	49.38	87.0	3.14

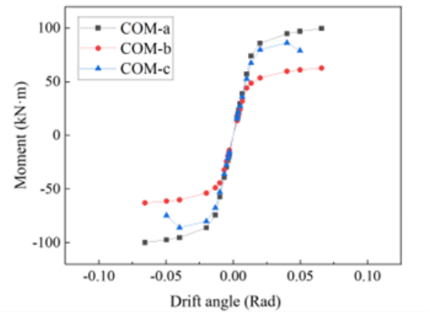

Fig. 20 Group COM backbone curves

4. Panel zone analytical flexural capacity

This section proposes an analytical method to calculate the flexural capacity of beam-through beam-column connections, which is validated by the numerical results received in previous sections. The following assumptions are adopted herein. First, the beam-column panel joints' flexural capacity is mainly provided by the beam-through web and the strengthening doubler plates. Thus, a rigid subframe comprises beam-through flanges, column end plates, and beam-through stiffener plates. Furthermore, a tensile area occurs when the beam-through web buckles, sloped 45° from the horizontal direction in parallel to the beam direction. Last, the impact of axial load on the flexural capacity of beam-column connections is ignored. The analytical beam-through beam-column connection panel joint is sketched in Fig. 21.

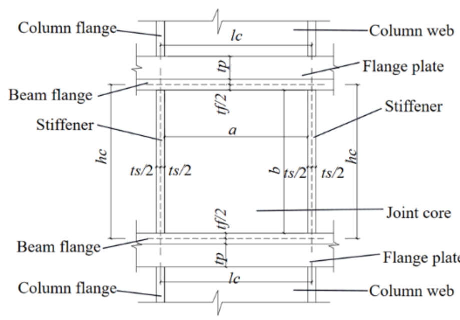

Fig. 21 Joint Panel zone design parameters

Fig. 22 shows the analytical force distribution in a beam-through beam-column panel zone. The beam and column end shear forces compose the moment and shear forces in the panel zone area (Figs. 22a and 22b). The beam-end panel zone moments (M_1) cause a pair of forces V_{m1} in the opposite directions along the beam flanges, and the column-end panel zone moment (M_2) induces another pair of forces in the opposite directions along the beam stiffener plates, as in Fig. 22c. The two pairs of opposite forces denote the perimeter forces around the rigid subframe panel zone area (Fig. 22e). Under the interactions of the shear forces around the panel zone, the beam-through web is in shear actions, which can be seen in Fig. 22f.

The analytical equation to calculate joint panel zone moment capacity can be conducted by analyzing Fig. 21 to 22 as in Eq. 5 to 6.

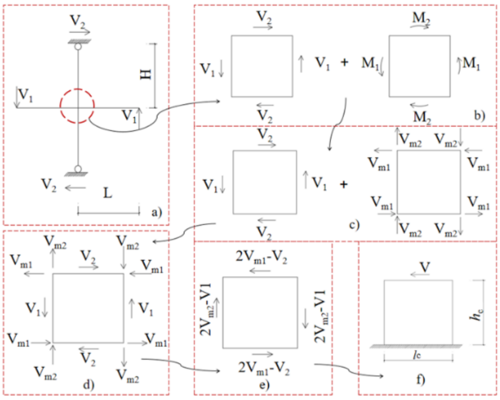

Fig. 22 Joint Panel zone force distribution and diaphragm

$$M_1 = V_1\left(L - \frac{l_c}{2}\right) = V_{m1}h_c \tag{5}$$

$$M_2 = V_2\left(H - \frac{h_c}{2}\right) = V_{m2}l_c \tag{6}$$

By performing moment equilibrium in the panel zone, the following equation is summarized.

$$V_1L = V_2H \tag{7}$$

Furthermore, Eq. 8 can be achieved by running force equilibrium.

$$V = 2V_{m1} - V_2 = 2V_{m2} - V_1 \tag{8}$$

By incorporating Eqs. 5, 6, 7 into Eq. 8,

$$V = V_1\frac{2HL - Lh_c - Hl_c}{Hh_c} = V_2\frac{2HL - Lh_c - Hl_c}{Ll_c} \tag{9}$$

The principal stress distribution diagram in the joint panel zone area is shown in Fig. 23a. σ_t, σ_c denotes the principal tensile and compressive stress. The horizontal and vertical stresses in the panel zone steel plate are shown in Figs. 23b and 23c, where σ_{yx} is the shear stress in the horizontal stress component, and θ represents the angle between the tensile stress and the horizontal direction along the through-beam longitudinal direction. The boundary shear and normal stress can be deduced below by performing stresses tensor notation $\sigma'_{mn} = \sigma_{ij}n_{mi}n_{nj}$.

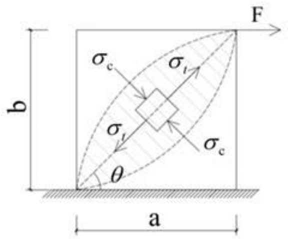

(a) Web principal stress distribution

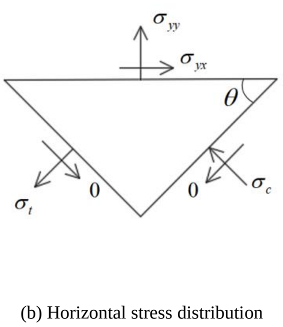

(b) Horizontal stress distribution

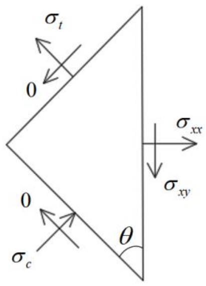

(c) Vertical stress distribution

Fig. 23 Through-beam web stress distribution

$$\sigma_{xy} = \sigma_{yx} = \frac{1}{2}(\sigma_t + \sigma_c)sin2\theta \tag{10}$$

$$\sigma_{xx} = \sigma_t cos^2\theta - \sigma_c sin^2\theta \tag{11}$$

$$\sigma_{yy} = \sigma_t sin^2\theta - \sigma_c cos^2\theta \tag{12}$$

A tension strip is developed as the beam-through web buckles. Then, the tensile stress becomes uniform, and σ_c equals zero. Referring to the conclusions and recommendations provided by Driver et al. [49] and Elgaaly et al. [50], the inclination angle for the tensile strip in the rigid subframe located in the beam-through beam-column connection is roughly 45°. Thus, Eq. 13 can be summarized by following the von Mises yield criterion [51], where f_y is the steel plate yield strength.

$$(\sigma_{xx} - \sigma_{yy})^2 + \sigma_{yy}{}^2 + \sigma_{xx}{}^2 + 6\sigma_{xy}{}^2 = 2f_y{}^2 \tag{13}$$

The following equations can be compiled by adding Eqs. 10, 11, and 12 into Eq. 13.

$$\sigma_{xy} = \frac{1}{2}f_y \tag{14}$$

Taking the web shear yielding strength $F_u = \sigma_{xy}at_w$ into Eq. 14 leads to the calculation of F_u. A modification factor, μ is adopted into Eq. 15 to reduce the error induced by ignoring the axial load effects. Where a is the panel zone horizontal length in the beam-through direction, t_w represents the panel zone web thickness.

$$F_u = \frac{1}{2}\mu f_y a t_w \tag{15}$$

The panel zone strengthening doubler plates are considered by adopting a doubler strength modification factor because the doubler plates are attached to the panel zone by welding the plate edge and another nine welding points with limited capacities. f'_y is the doubler plate strength, and t'_w denotes the doubler plate thickness.

$$F_u = \frac{1}{2}a(\mu f_y t_w + \beta f'_y t'_w) \tag{16}$$

Assume $F_u = V$,

$$V_1 = \frac{Hh_c a(\mu f_y t_w + \beta f'_y t'_w)}{4HL - 2Lh_c - 2Hl_c} \tag{17}$$

Consider the panel zone moment capacity is $M_u = V_1L$.

$$M_u = \frac{Hh_c La(\mu f_y t_w + \beta f'_y t'_w)}{4HL - 2Lh_c - 2Hl_c} \tag{18}$$

By further analyzing all the numerical results in section 3 and performing design parameter regression, the modification factor, α equals 1.28, and β can be calculated as follows:

$$\beta = 0.53\gamma^2 - 1.72\gamma + 2.31 \tag{19}$$

$$\gamma = \frac{f'_y t'_w}{f_y t_w} \tag{20}$$

Where γ is the doubler plate strength ratio that denotes the ratio of doubler plate strength over panel zone web strength. Table 9 provides all computational parameters and sample results for all the specimens designed in previous sections. As observed, the analytical method and equations presented in this section can successfully predict the flexural capacity of the panel zone in beam-through beam-column connections. The maximum difference between the analytical and numerical results is 2.47%. Consequently, the proposed analytical equations can be utilized to simulate the flexural capacity for beam-through beam-column moment connections in steel structural design and other earthquake engineering simulations.

With all the equations derived, it is worth noting that they apply not only to the panel zone of beam-through joints but also to the panel zone of traditional column-through beam-column joints. Since the post-yielding tensile band is assumed to maintain a 45° angle from the horizontal direction, the analytical method can accurately predict the panel zone flexural capacity in any square area. When the panel zone is not a square (i.e., width is not equal to height), the angle between the post-yield tensile band is no longer 45°, when the current analytical method might not be accurate. As the panel zone height-to-width ratio increases, multiple tensile bands may occur, which is totally ignored in this study. However, multiple tensile bands and angles in the panel zone are more complicated topics, requiring further investigation.

5. Conclusions

This study performs numerical and analytical investigations of the flexural behaviors of beam-through H-section (wide-flange) steel beam-column moment-resisting connections. Beam-through beam-column joints can accelerate construction progress by lifting and erecting a portion or even a floor of building structures. Thus, a large portion of sophisticated welding can be performed in factories or on the ground, expediting the completion of complex weld connections with good quality assurance or quality control (QA/QC). In addition, shop welding and modular field erection significantly reduce field labor costs, making this approach highly marketable with promising engineering application possibilities compared to other methods.

Five types of reinforcing methods or combinations are considered. Finally, an analytical method is proposed to calculate the seismic flexural capacity of through-beam beam-column joints. The main findings are summarized below:

1. The thickness of web stiffener plates in through-beam beam-column joints has negligible effects on the joint seismic performance. However, it is still recommended to design the through-beam web stiffener plate not thinner than the column flanges, which aims to transfer the column axial loads through the through beam efficiently.

2. Increasing the doubler plate thickness and strength can both effectively improve the yield and ultimate capacities of beam-through beam-column connections, where the former method is superior.

3. The American Institute of Steel Construction (AISC) prequalified (reduced beam section) RBS can still shift the possible weak points and plastic hinges outside the connection panel zones. Furthermore, this study strongly recommends engineers to calculate the seismic capacity at the beam-column panel zones and RBS, which intends to fully engage the RBS configuration. Also, RBS reduces not only the beam-column joint capacity but also its ductility in the through-beam design.

4. Combining the through-beam beam-column joint doubler plates with RBS can adequately transfer the weak zone and plastic hinges from the joint panel zone to the beam ends, which satisfies the design concept in the current building seismic codes.

5. The proposed simplified analytical method and equations derived from force equilibrium, stress tensor rotation, and von Mises yield criterion can accurately predict the flexural capacity for beam-through beam-column panel joints. This method provides technical and design support for steel seismic-resisting structures with beam-through steel moment frames.

Table 9

Comparison of numerical and analytical results

Name	Beam web strength f_y (MPa)	Beam web thickness t_w (mm)	Doubler plate strength f'_y (MPa)	Doubler plate thickness t'_w (mm)	Doubler plate strength ratio $\gamma = \frac{f'_y t'_w}{f_y t_w}$	Numerical yield moment M'_u (kN.m)	Analytical yield moment M_u (kN.m)	Difference
SFT-6	369	6	0	0	0	47.72	47.53	-0.40%
DPT-2	369	6	300	2	0.27	57.50	56.08	-2.47%
DPT-4	369	6	300	4	0.54	66.84	68.00	1.73%
DPT-6	369	6	300	6	0.81	74.64	75.23	0.79%
DPT-8	369	6	300	8	1.08	80.29	80.13	-0.19%
DPT-10	369	6	300	10	1.36	84.29	85.06	0.91%
DPS-300	369	6	300	6	0.81	74.64	75.23	0.79%
DPS-360	369	6	360	6	0.98	78.30	78.30	0.00%
DPS-420	369	6	420	6	1.14	81.69	81.04	-0.79%

References

[1] Ding Y., Deng E.F., Zong L.,Dai X.M., Lou N., and Chen Y. "Cyclic tests on corrugated steel plate shear walls with openings in modularized-constructions", Journal of constructional steel research, 138, 675-691, 2017.

[2] Yin X., Liu H., Chen Y., and Al-Hussein M. "Building information modelling for off-site construction: Review and future directions", Automation in construction, 101, 72-91, 2019.

[3] Liu X.C., Pu S.H., Zhang A.L., and Zhan X.X. "Performance analysis and design of bolted connections in modularized prefabricated steel structures", Journal of Constructional Steel Research, 133, 360-373, 2017.

[4] Zhang A.L., Shangguan G.H., Zhang Y.X., Wang Q.B., and Cai W.C. "Experimental study of resilient prefabricated steel frame with all-bolted beam-to-column connections", Advanced Steel Construction, 16(3), 255-271, 2020.

[5] Chu Y.P., Chen X.Q., Zhong Y., and Zhang H.C. "Seismic fragility analysis of steel frames with fully-bolted core tube joints", Advanced Steel Construction, 20(3), 208-221, 2024.

[6] Zhang X., Zhou B., Gao J.D., Qian H., Song L.Z., and Cai L.M. "Numerical investigation on seismic performance of prefabricated steel beam-to-column connection with replaceable U-shaped plate", Advanced Steel Construction, 20(4), 7-405, 2024.

[7] Zhang Z.W., Li D., Wang H.J., Qian H.L., Fang W.Q., Jing X.F., and Fan F., "Study of mechanical properties of a novel column-beam-column prefabricated steel frame joint", Advanced Steel Construction, 20(4), 0-344, 2024.

[8] Qin Y., Chen Z., Wang X., and Zhou T. "Seismic behavior of through-diaphragm connections between CFRT columns and steel beams-experimental study", Advanced Steel Construction, 10(3), 351-371, 2014.

[9] Rong B., Zhang Y., Sun J., and Zhang R. "Experimental and numerical research on hysteretic behavior of CFST frame with diaphragm-through connections", Journal of Building Engineering, 45, 103529, 2022.

[10] Wu L., Wang X., Luo S., Wang X., Cui D., and Chen, Z. "Experimental research on seismic performance of the full-bolted diaphragm-through connection to RCFST", Advances in Structural Engineering, 18(7), 959-973, 2015.

[11] Wang W., Hu S.L., Zou C., and Chen Y.S. "The effects of joint behavior on the seismic performance of floor-by-floor assembled steel beam-through braced frames", Engineering Mechanics, 36(4), 206-213, 2019 (In Chinese).

[12] Wang W., Zhou Q., Chen Y., Tong L.W., and Chan T.M. "Experimental and numerical investigation on full-scale tension-only concentrically braced steel beam-through frames", Journal of Construction Steel Research, 80, 369-385, 2013.

[13] Yao Z.C., Wang W., Fang C., and Zhang Z.Y. "An experimental study on eccentrically braced beam-through steel frames with replaceable shear links", Engineering Structures, 110185, 2020.

[14] Xi Que Wu. 2023. http://www.xiquewu.cn/2020/12/5465/

[15] Sekisui Heim. Factory Production system. 2022. https://www.sekisuichemical.com/about/division/housing/index.html

[16] Chen Y.S., Wang W., and Chen Y.Y. "High-strength steel for resilience of beam-through frames", Proceedings of the Institutution of Civil Engineering Structures and Building, 170(9), 2017.

[17] Chen Y.S., Wang W., and Chen Y.Y. "Full-scale shake table tests of the tension-only concentrically braced steel beam-through frame", Journal of Constructional Steel Research, 148, 611-626, 2018.

[18] Dong B.P., Chen Y.S., and Wang W. "Self-centering mechanism and seismic response of steel tension-only concentrically braced beam-through frames", Structures, 30, 960-972, 2021.

[19] Hu S.L., Wang W., and Qu B. "Enhancing seismic performance of tension-only concentrically braced beam-through frames through implementation of rocking cores", Engineering Structures, 169, 68-80, 2018.

[20] Hu S., Wang W., Alam M.S., and Qu B. "Improving the Seismic Performance of Beam-through Concentrically Braced Frames Using Energy-absorbing Rocking Core", Journal of Earthquake Engineering, 26(7), 2022.

[21] Zhang R.B., Wang W., Yang C.Y., Hu S.L., and Shahria A.M. "Hybrid test and numerical study of beam-through frame enhanced by friction spring-based self-centering rocking core", Engineering Structures, 274, 115157, 2023.

[22] Li J.L., Wang W., and Li P.Y. "Development and experimental study of steel beam-through framed connections with T-type curved knee braces for improving seismic performance", Engineering Structures, 231, 111722, 2021.

[23] Li J.L., Wang W., and Li P.Y. "Development, testing and performance evaluation of steel beam-through framed connections with curved knee braces for improving seismic performance", Journal of Constructional Steel Research, 179, 106552, 2021.

[24] Li Y.W., Wang Y.Z., and Wang Y.B. "Experimental and numerical study of beam-through energy-dissipative rocking columns for mitigating seismic responses", Journal of Constructional Steel Research, 189, 107097, 2022.

[25] Jeddi M.Z., Sulong N.H.R., and Khanouki M.M.A. "Seismic performance of a new through rib stiffener beam connection to concrete-filled steel tubular columns: An experimental study", Engineering Structures, 131, 477-491, 2017.

[26] Jamali P.F., Ali H.M., and Hamed S. "Seismic behavior of through beam connection to steel box-column", Journal of Constructional Steel Research, 193, 107261, 2022.

[27] Chen Z.H., Niu X.Y., Liu J.D., Khan, K., and Liu Y.C. "Seismic study on an innovative fully-bolted beam-column joint in prefabricated modular steel buildings", Eng Struct 2021; 234, 111875.

[28] Tagawa H. and Gurel S. "Application of steel channels as stiffeners in bolted moment connections", Journal of Constructional Steel Research, 61(12), 2005.

[29] Zhong W.H., Zhao M.J., Zhou L., Tan Z., Sun W., and Zheng Y.H. "Seismic performance of a narrow flange H-beam-to-column full-bolt end-plate weak-axis connection", Structures, 46, 637-653, 2022.

[30] Čermelj B., Može P., and Sinur F. "On the prediction of low-cycle fatigue in steel welded beam-to-column joints", Journal of Constructional Steel Research, 117, 49-63, 2016.

[31] Ma H.W., Zheng H., and Zhang W. "Experimental and numerical study of mechanical properties for the double-ribbed reinforced beam-column connection", Advanced Steel Construction, 16(4), 297-309, 2020.

[32] Du H.K., Zhao P.F., Wang Y.D., and Sun W.T. "Seismic experimental assessment of beam-through beam-column connections for modular prefabricated steel moment frames", Journal of Constructional Steel Research, 192, 107208, 2022.

[33] Chen S.J., Yeh C.H., and Chu J.M. "Ductile steel beam-to-column connections for seismic resistance", Journal of Structural Engineering, 122(11), 1292-1299, 1996.

[34] Sophianopoulos D.S. and Deri A.E. "Parameters affecting response and design of steel moment frame reduced beam section connections: an overview", International Journal of Steel Structures, 11, 133-144, 2011.

[35] Carter C.J. and Iwankiw N.R. "Improved ductility in seismic steel moment frames with dogbone connections", Journal of Constructructional Steel Research, 1(46), 448, 1998.

[36] Jones S.L., Fry G.T., and Engelhardt M.D. "Experimental evaluation of cyclically loaded reduced beam section moment connections", Journal of Structural Engineering, 128(4), 441-451, 2002.

[37] Lee C.H., Jeon S.W., Kim J.H., and Uang C.M. "Effects of panel zone strength and beam web connection method on seismic performance of reduced beam section steel moment connections", Journal of Structural Engineering, 131(12), 1854-1865, 2005.

[38] Wang H.T., Huo J.S., Elchalakani M., Liu Y.Z., and Zhang S.Q. "Dynamic performance of retrofitted steel beam-column connections subjected to impact loadings", Journal of Constructructural Steel Research, 183, 106732, 2021.

[39] Chen C.W., Qiao H.Y., Wang J.P., and Chen Y. "Progressive collapse behavior of joints in steel moment frames involving reduced beam section", Engineering Structures, 225, 111297, 2020.

[40] Roudsari M.T., Abdollahi F., Salimi H., Azizi S., and Khosravi A.R. "The effect of stiffener on behavior of reduced beam section connections in steel moment-resisting frames", International Journal of Steel Structures, 15, 827-834, 2015.

[41] General Administration of Quality Supervision, Inspection and Quarantine of China, Standardization Administration of China. The hot-rolled H and cut T section steel (GB/T 11263-2017). Beijing, China, 2017.

[42] AISC. Steel Construction Manual 15th ed. American Institute of Steel Construction, Chicago, IL, 2017.

[43] AISC 341. Seismic Provisions for Structural Steel Buildings, Chicago, IL, 2016.

[44] Wang Y.D., Ibarra L., and Pantelides C. "Collapse capacity of reinforced concrete skewed bridges retrofitted with buckling-restrained braces", Engineering Structures, 184, 99-114, 2019.

[45] Wang Y.D., Ibarra L., and Pantelides C. "Seismic retrofit of a three-span RC bridge with buckling-restrained braces", ASCE Jounral of Bridge Engineering, 21(11), 04016073, 2016.

[46] Ministry of Housing and Urban-Rural Development of China. Standard for design of steel structures. (GB50017-2017). Beijing, China, 2017.

[47] AISC 358. Prequalified connections for special and intermediate moment frames for seismic application. Chicago: American Institute of Steel Construction; 2016.

[48] GB 50011-2016. Code for seismic design of buildings. Ministry of Housing and Urban-Rural Development, Beijing, China, 2016.

[49] Driver R.G., Kulak G.L., Kennedy D.L., and Elwi A.E. "Cyclic test of four-story steel plate shear wall", Journal of Structructural Engineering, 124(2), 112-120, 1998.

[50] Park H.G., Kwack J.H., Jeon S.W., Kim W.K., and Choi I.R. "Framed steel plate wall behavior under cyclic lateral loading", Journal of Structructural Engineering, 133(3), 378-388, 2007.

[51] Yang L.T. Introduction to Elastoplastic Mechanics, Tsinghua University, Beijing, China, 2013.